Design and analysis of multi-color confocal microscopy with a wavelength scanning detector

Dukho Do, Wanhee Chun, and Dae-Gab Gweon

Related Articles

Dilation x-ray imager a new/faster gated x-ray imager for the NIF
Rev. Sci. Instrum. 83, 10E116 (2012)

A magnifying fiber element with an array of sub-wavelength Ge/ZnSe pixel waveguides for infrared imaging
Appl. Phys. Lett. 101, 021108 (2012)

Low cost alternative of high speed visible light camera for tokamak experiments
Rev. Sci. Instrum. 83, 10E505 (2012)

Ultra fast x-ray streak camera for ten inch manipulator based platforms
Rev. Sci. Instrum. 83, 10E106 (2012)

X-ray bang-time measurements at the National Ignition Facility using a diamond detector
Rev. Sci. Instrum. 83, 10E105 (2012)
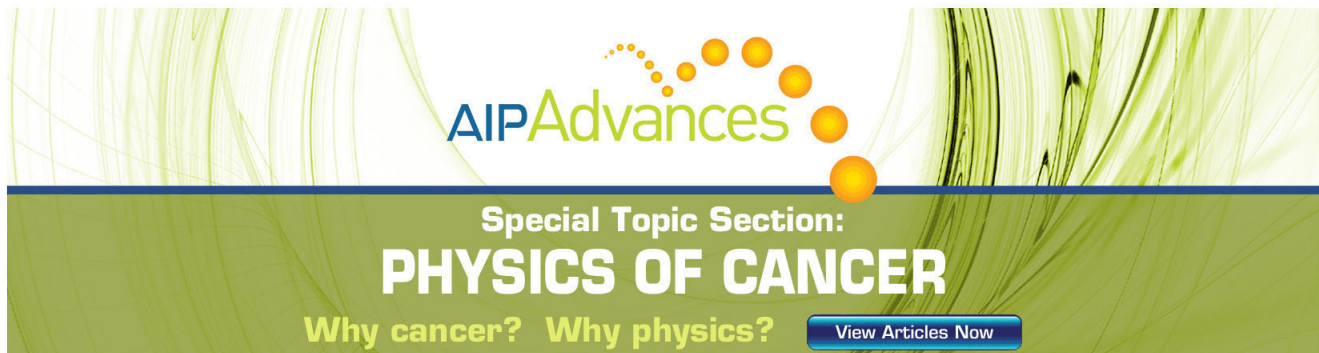
Additional information on Rev. Sci. Instrum.

Design and analysis of multi-color confocal microscopy with a wavelength scanning detector

Dukho Do, Wanhee Chun, and Dae-Gab Gweon
Department of Mechanical Engineering, KAIST, Dae-jeon 305-701, Korea

Spectral (or multi-color) microscopy has the ability to detect the fluorescent light of biological specimens with a broad range of wavelengths. Currently, the acousto-optic tunable filter (AOTF) is widely used in spectral microscopy as a substitute for a multiple-dichroic mirror to divide excitation and emission signals while maintaining sufficient light efficiency. In addition, systems which utilize an AOTF have a very fast switching speed and high resolution for wavelength selection. In this paper, confocal-spectral microscopy is proposed with a particular spectrometer design with a wavelength-scanning galvano-mirror. This enables the detection of broadband (480–700 nm) fluorescence signals by a single point detector (photomultiplier tube) instead of a CCD pixel array. For this purpose, a number of optical elements were applicably designed. A prism is used to amplify the dispersion angle, and the design of the relay optics matches the signals to the diameter of the wavelength-scanning galvano-mirror. Also, a birefringent material known as calcite is used to offset the displacement error at the image plane depending on the polarization states. The proposed multi-color confocal microscopy with the unique detection body has many advantages in comparison with commercial devices. In terms of the detection method, it can be easily applied to other imaging modalities. © *2012 American Institute of Physics*. [http://dx.doi.org/10.1063/1.4717679]

I. INTRODUCTION

The multi-color confocal microscope has the ability to detect multiple colors. Wavelength dependent images such as the fluorescence spectrum can be obtained with this system. It is often important to obtain the spectrum information of biological samples.[1] Multiple stained fluorescent dyes or fluorescent proteins can be detected via its multi-color microscope techniques.[2,3] This advantage is used with various biological applications compared to a conventional microscope.

Multi-color confocal microscopes have been developed by a number of major microscope companies as commercial products. The basic structure has an acousto-optic tunable filter (AOTF) that divides its excitation and emission light. That is, the AOTF acts as a dichroic mirror. Its RF signal makes the excitation light diffract in a direction of a +1 or −1 order. The fluorescence light from the samples emits unpolarized light, which is in a state of broken polarization compared to the original status. Also, the fluorescent light does not diffract as the excitation light does. Due to the different light paths between the excitation and the emission light, fluorescence detection is possible. The light passing through the AOTF propagates to the dispersion element to disperse the signal. Its spectrometer designs vary depending on the application.

The Leica Corp. and other groups have developed confocal-spectral microscopy, which has moving slits and photomultiplier tubes (PMTs).[4–7] By adjusting the width and position of the slits, the detection band can be freely changed. Especially for the products created by Leica, simultaneous detection is possible due to the use of multiple PMTs. With such a microscope, users can easily tune the detection wavelength. However, the wavelength switching time is limited by the actuation of the slit, which is not fast enough for spectral-imaging. The Nikon C1si (Ref. 8) is another confocal-spectral microscope. The fluorescence signal is dispersed by a grating and the dispersed light is then simultaneously detected by the multi-channel PMT. Due to its multi-channel detection capability, spectral imaging at a high speed is possible. However, the number of channels is limited and ultimately cannot be increased.[9] Therefore, there is a trade-off between the wavelength range and spectral resolution.

In this paper, the weak points mentioned above are complemented by designing a spectral-detecting system via a different concept. Instead of a slit, wavelength selection is done by rotating a galvano-mirror and a single PMT. Compared to the moving-slit type, the wavelength switching time is increased without any constraint on the wavelength range. The system is limited by the settling time of the galvano mirror, which is 200 μs (two extreme wavelengths) in our experiment setup. Thus, it is faster than the moving slit type and continuous spectral detection is possible. The spectral resolution can be adjusted by changing the prism through a change in the amplification. If a prism having a large dispersion angle is used, the spectral resolution can be enhanced at even the sub-nanometer level. For simultaneous detection with a multi-channel PMT, the measurable wavelength range becomes narrower after enhancing the spectral resolution due to the limited channels. In our method, a wide range of wavelengths can be obtained simply by rotating the galvano-mirror. The maximum scanning angle (typ. $\pm 20°$), which is quite sufficient for the scanning of the entire wavelength, facilitates high-resolution spectral imaging with a wide range of wavelengths.

TABLE I. Design parameters and results of the relay lens system.

Design parameters	Results
Wavelength	480–700 nm
Beam diameter	2.9 mm
Scanning angle	$\pm 4.2°$
Magnification	$\times 3$
Total length	210 mm
Longitudinal aberration	$<1.2 \mu$m (from 480 to 700 nm)
RMS wavefront error	$<0.046\lambda$

Another advantage of using the proposed spectral detection method is that it is easy to combine other imaging modalities such as FLIM (fluorescence lifetime imaging microscopy), FCS (fluorescence correlation spectroscopy), or TPM (two-photon microscopy).[10] For example, FLIM is a method used to measure the fluorescence lifetime. It usually uses a time-correlated single-photon counting board connected to a photomultiplier tube(PMT). It is difficult to extend the number of detecting channel beyond 4.[4,11–13] If multiple PMTs are used (up to 4), the entire system becomes complex and expensive when trying to obtain spectral FLIM images.

II. BIREFRINGENCE IN AOTF

$$\text{Efficiency } \eta(\%) = \frac{I_{1st}}{I_{1st}+I_{0th}} \times 100. \qquad (1)$$

The AOTF was developed by Brillouin, who initially predicted that light scattering can be caused by acoustic wave.[14] In addition, a non-collinear birefringent material known as TeO_2 was originally utilized as an AOTF by Chang.[15] An AOTF can be utilized as a beam splitter, as shown in Fig. 1(a). Due to the use of the AOTF as a dichroic mirror, the birefringent characteristic has to be counterbalanced.[16] The emission light from any fluorophore is incoherent, and it has two orthogonal polarization states even if it absorbs linearly polarized light. When the emission light from the specimen passes the AOTF in an un-polarized state, the refractive indices differ due to the birefringence of the AOTF material. Therefore, the two types of polarized light propagate at different dispersion angles as shown in Fig. 1(b). Regarding the AOTF as a prism with an apex angle of α, the dispersion angle of the fluorescent light can be calculated as follows:[17]

$$\delta = \sin^{-1}[(\sin\alpha)\sqrt{n^2 - \sin^2\theta_i} - \sin\theta_i\cos\alpha]. \qquad (2)$$
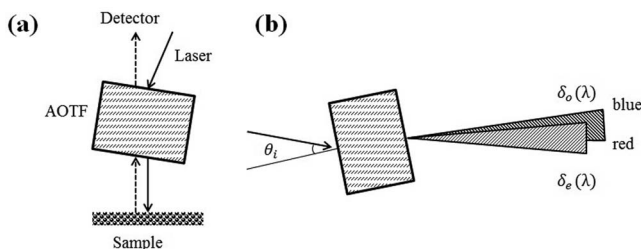

FIG. 1. (a) Schematic of the AOTF used as a dichroic beam splitter (known as an AOBS). (b) The propagation of fluorescent light with a different dispersion angle depending on the polarization state and wavelength.
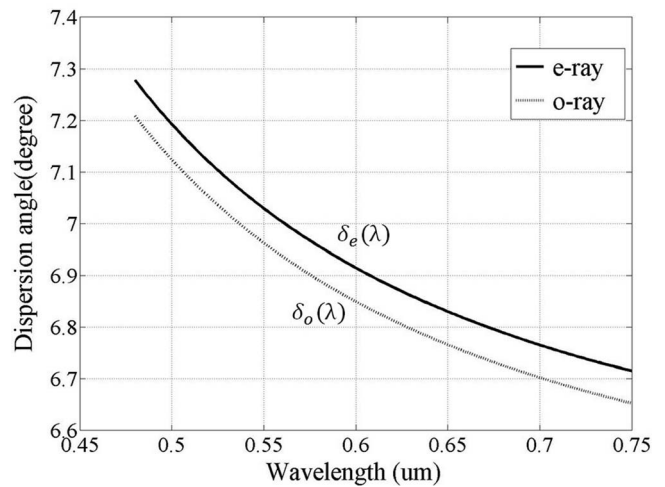

FIG. 2. The dispersion angle of the o-ray (dotted line) and the e-ray (solid line) is depicted.

In this equation, the refractive index n is related to the wavelength and the polarization state. Among the two polarization states, the isotropic polarization state is called the o-ray state. The other state is called the e-ray state. This indicates that incident light at a certain angle will experience different refractive index values depending on the polarization state. According to Eq. (2), the dispersion angle of the two polarization states is calculated as follows:

$$\delta_{e,o} = \sin^{-1}[(\sin\alpha)\sqrt{n_{e,o}^2 - \sin^2\theta_i} - \sin\theta_i\cos\alpha]. \qquad (3)$$

Equation (3) is plotted in Fig. 2. Similar smooth curves are depicted between the two polarization states. The difference angle of the o-ray and e-ray states as a nearly constant value. This difference causes a lateral mismatch of the focal point at the detector. By inserting an additional birefringent crystal, known as calcite, the displacement can be offset as shown Fig. 3. While varying the thickness of the calcite, the amount of focal shift changes. After some amount of ray tracing of the designed lens systems, the thickness of the calcite was determined.

The actual beam spots after passing through the AOTF are depicted as shown in Fig. 4. Most of the incident beam is diffracted and propagates on a first-order path, but there
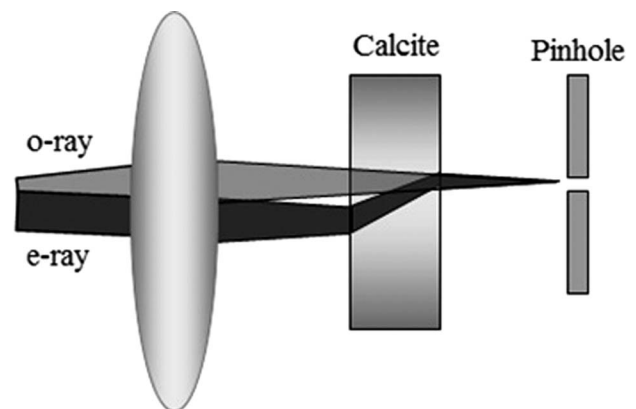

FIG. 3. Compensation of the o-ray and e-ray states is done using calcite.
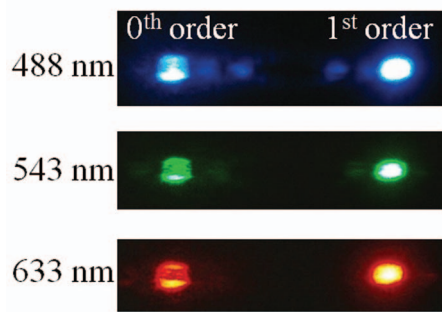
FIG. 4. Actual beam spots are captured after passing the AOTF. Input laser beams are divided in zeroth- and first-order beams.
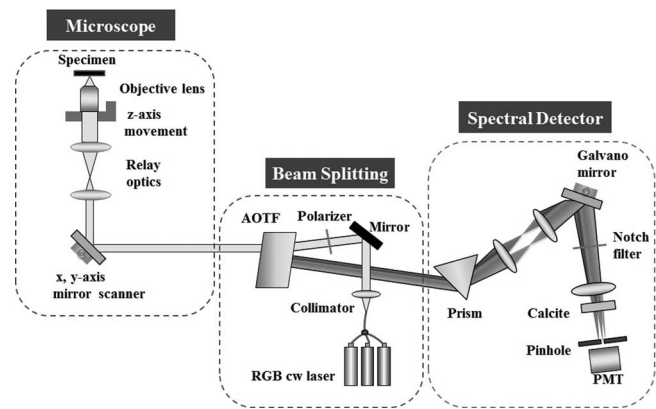

FIG. 6. The system implementation is depicted. The designed system is composed of the microscope part, the beam splitting part, and the spectral detector part.

exists a zeroth-order beam as well. The diffraction efficiency of the AOTF can be calculated by Eq. (4). When an input beam having a total intensity of $I_{1st} + I_{0th}$ enters, it is divided into two beams. One is the diffracted beam (I_{1st}) and the other is the un-diffracted beam (I_{0th}). The intensity of the diffracted beam was measured according to its incident angle and three types of excitation lasers. The corresponding RF frequencies are also plotted in Fig. 5 simultaneously. In the vicinity of the actual incident angle, the diffraction efficiencies were found to be greater than 90%. These values do not lead to any problems for the reason that the intensity was quite appropriate for exciting any fluorescent material. Moreover, the first-order beam is slightly distorted, but this factor does not affect the performance. There are several factors that allow this. First, the edge of the beam is cut out at the back aperture of the objective lens. In addition, the usage of a pinhole acts to purify the distorted beam.

III. SYSTEM DESIGN AND IMPLEMENTATION

The entire system can be divided into three parts (see Fig. 6). First, the microscope part has an objective lens, relay optics, and x- and y-axis mirror scanners. The fast-axis scanner is an 8 kHz resonant scanner by GSI Group Inc. The

design of the relay optics has a wavelength range of 480 nm–700 nm and a field of view of $200\mu m \times 200\mu m$ with a 40× Olympus objective lens. The z-axis piezoelectric transducer uses the MIPOS 500 device of Thorlabs. Second, the beam splitting part is composed of an AOTF, three lasers, and a collimator. A 488 nm Ar-ion laser and 543 nm and 633 nm He–Ne lasers are combined into one fiber and collimated with a diameter of 3 mm. After passing the polarizer, the collimated light propagates to the AOTF. With the appropriate RF signal of the AOTF, the specific wavelength of the lasers is diffracted into the microscope part. Finally, the spectral detector part has a prism, a galvano-mirror, the calcite, a PMT detector, and supporting parts. The prism is used to amplify the dispersion angle for spectral detection. The lens system in front of the galvano-mirror reduces the beam size, i.e., it collects dispersed light in the galvano-mirror. By rotating the galvano-mirror, the wavelength band can be selected. Continuous wavelength detection is also possible. A notch filter is used to block the laser wavelength perfectly. A picture of the actual system is presented as shown in Fig. 7.
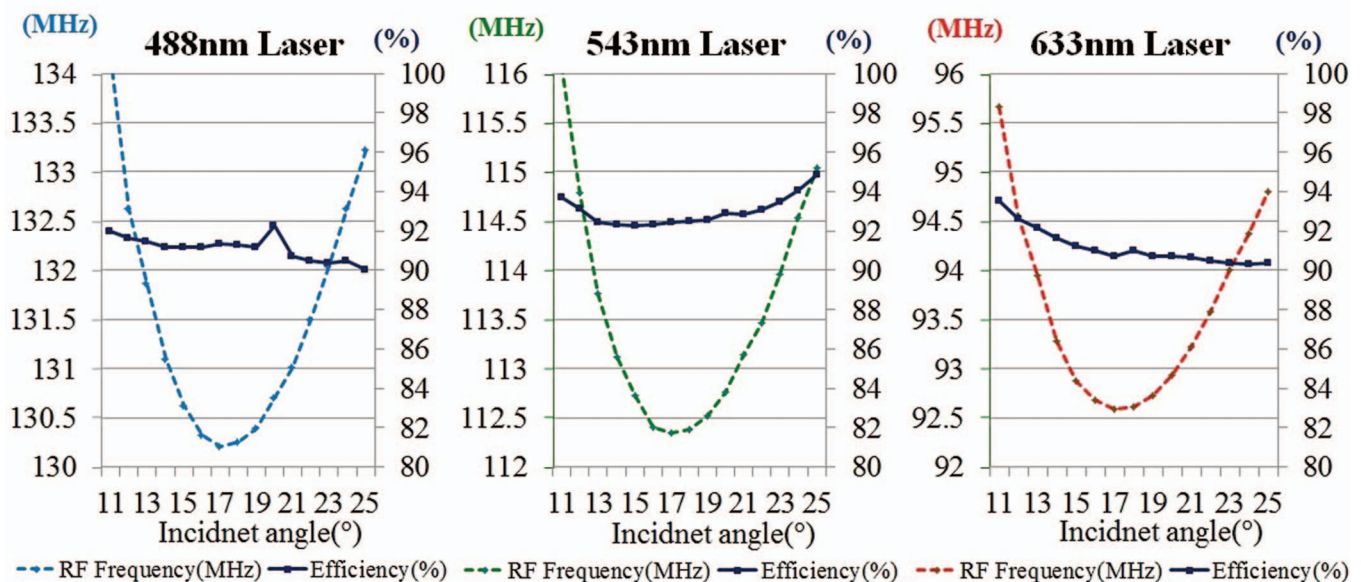

FIG. 5. The light efficiency of the AOTF and the corresponding RF frequency are plotted.
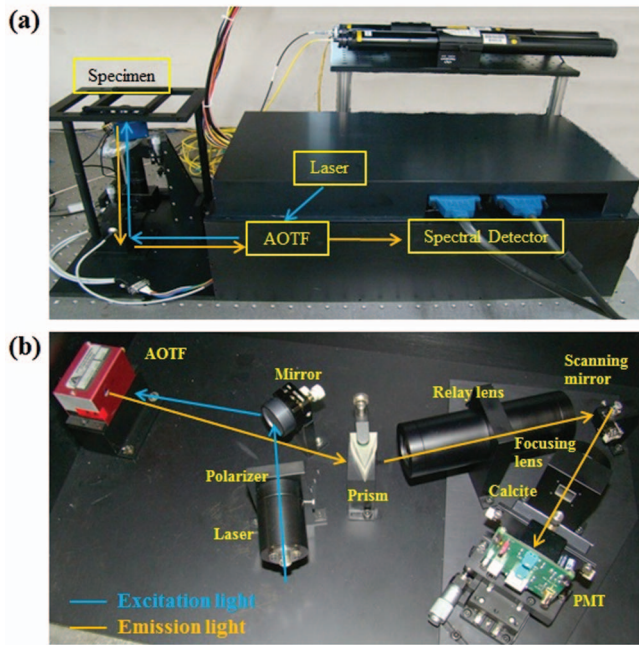
FIG. 7. A picture of the actual system is presented. (a) is the entire microscope system. The detection part is sealed with an aluminum frame to block the background light. (b) is the detection part inside the frame. The path of the excitation and emission light is depicted with different colors.

We designed the relay lens, which is composed of a scan and a tube lens system according to design parameters listed as Table I. The relay lens has six single lenses which are arranged as shown in Fig. 8(a). The spot diagram in Fig. 8(b) shows that all of the spots focused on the image plane are inside its airy disk. This tells us that the design of the relay lens leads to good performance. Also, the longitudinal aberration depending on the wavelength is plotted in Fig. 8(c). The overall wavelength range is from 480 nm to 700 nm, and the longitudinal aberration is below 1.2 μm. This value may affect the axial resolution of a conventional confocal microscope, especially at both ends of its wavelength. However, it is inescapable and the relay lens was carefully designed to minimize any longitudinal aberrations. Also, this is no critical when imaging a biological specimen.

The design of the spectral detector is shown below in considerable detail (see Fig. 9). In the detailed design procedure,
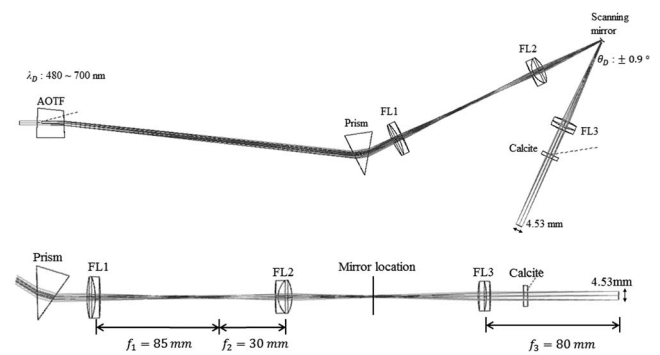
FIG. 9. The detail design of the spectral detector is described. λ_D is wavelength range of the collection light. f_i is the focal length of the ith doublet lens. θ_D is scanning angle of the rotating mirror.

the distance between the AOTF and the prism was fixed at 215 mm. This spatial constraint is due to the perfect division of excitation/emission light. If the distance becomes smaller, some vignetting regions may appear due to the adjacent mirror. Another constraint is the angle difference between the e-ray and the o-ray states. By choosing the incident angle of the AOTF, the angle difference was fixed at 0.068°. The thickness of the calcite can be determined by this angle difference, and this was 3.0 mm. After some consideration, three types of lenses, FL1, FL2, and FL3, were selected as commercial doublet lenses. (Edmund Optics Inc.) These, respectively, have focal lengths of 85 mm, 30 mm, and 80 mm.

The simulation of the spot at the image plane was conducted as shown in Fig. 10. According to the wavelength, the offset between the o-ray and e-ray states can be observed. It has its maximum value at the lowest and highest wavelengths. However, all values are below 15 μm, which is smaller than the actual pinhole size. Therefore, the counterbalancing of the birefringence is possible with the use of only one birefringent material, though some non-linearity exists. On the other hand, the chromatic displacement of the focal plane from 480 nm to 700 nm is 1.956 mm. This value is quite small compared to the depth of focus. This is why we used a lens with a focal length of 80 mm in front of a pinhole and a beam diameter that was reduced by around 1 mm (NA $\approx$ 0.00625). This did not influence the accuracy of the optical sectioning.

IV. EXPERIMENTAL RESULTS

To verify the compensation of the birefringence, unpolarized laser light was illuminated, as shown in Fig. 11.
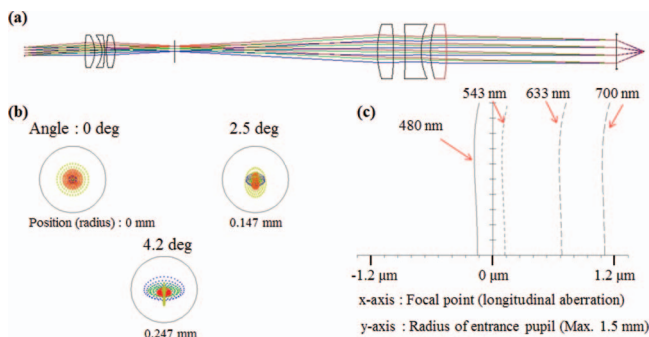

FIG. 8. The design result of the relay lens system. (a) Ray tracing through the scan lens and the tube lens. (b) Spot diagram at the image plane. (c) Longitudinal aberration of three representative wavelengths.
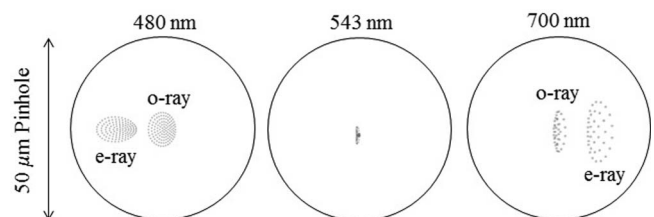

FIG. 10. The simulation of a spot diagram is described according to the actual pinhole size of 50 μm. The o-ray located at the center and e-rays with some degrees of offset are observed.
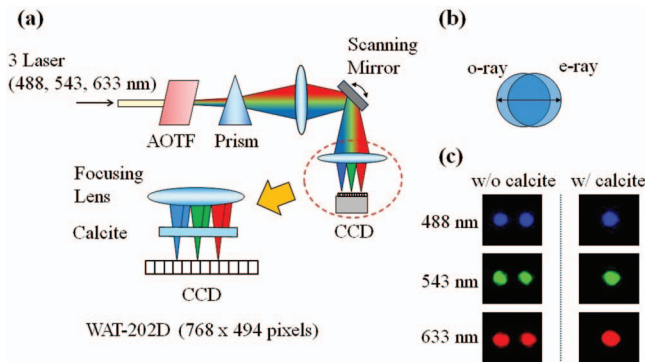
FIG. 11. The verification of compensation using a specific thickness of calcite is described. An experimental schematic is depicted in (a). Two polarized lights are overlapped as (b). CCD images of the spots are shown in (c).

Three types of lasers are incident on the AOTF to mimic the fluorescent light reflected from the sample. At the image plane, the PMT was replaced by a CCD camera to visualize the focusing spot. Without the calcite, two separated focusing spots were observed, as shown in Fig. 11(c). On the other hand, two spots were noted to be combined after the insertion of calcite having a specific thickness. As a result, the fluorescent signal is nearly doubled by combining the two orthogonal polarized lights.

To verify the amount of chromatic aberration of the wavelength-dependent images, images of the multi-color stained spheres are taken. Each specimen was dyed by three types of fluorescent materials. These were green, orange, and dark-red fluorescents. The images shown in Figs. 12(a)–12(c) were taken after the wavelength was chosen as the maximum emission wavelength of the each fluorescent. By rotating the scanning mirror, wavelength-dependent images were taken

from 480 nm to 700 nm. All of the images were mostly overlapped within the entire wavelength range. A mixed image of the images in Figs. 12(a)–12(c) is presented in Fig. 12(d). Lateral displacement of the object caused by the chromatic aberration was observed within three pixels, which is negligible compared to the overall number of pixels (512 pixels).

In addition, the frame rate of the proposed system is limited by the fastest scanning mirror, which is the resonant scanner of 8 kHz. If one image composed of 512 × 512 pixels is taken, the frame rate becomes 15.6 frame/s. Also, the wavelength-changing mirror has a settling time of 200 μs for the entire wavelength range. To obtain 50 types of different wavelength images, the total acquisition time would be 3.215 s:

$$\frac{50 \text{ frame}}{15.6 \text{ frame/s}} + 200\mu s \times 49 = 3.215s. \qquad (4)$$

A continuous spectrum signal can be obtained by the proposed system. To do this, three types of fluorescent beads are mixed on a slide glass: yellow-green beads with a 6-μm diameter, orange beads with a 6-μm diameter, and deep-red beads with a 1.5-μm diameter. The resulting emission peaks are 516 nm 561 nm, and 660 nm, respectively. Continuous wavelength-dependent images were taken by rotating the scanning mirror. Several representative images are presented in Figs. 13(a)–13(f). The labels of (b), (c), and (e) show the maximum emission wavelengths of each fluorescent bead. These can be mixed using the pseudo-colors shown in Fig. 13(g). The spectra of these fluorescent beads are depicted in Fig. 13(h). The solid lines refer to the measured intensity variation of each fluorescent bead depending
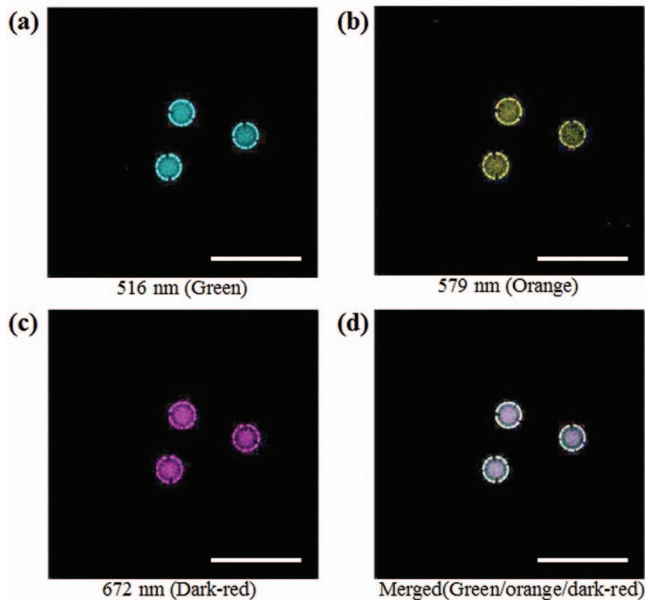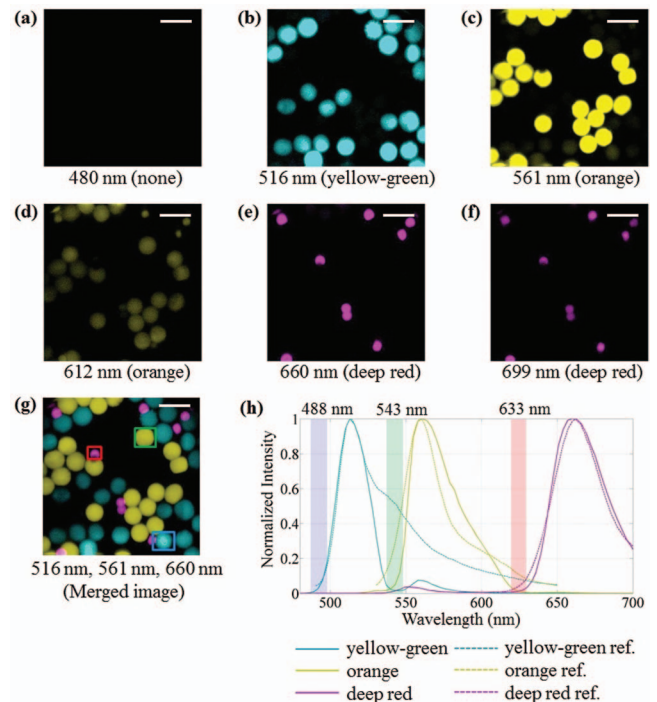

FIG. 12. The images of fluorescent spheres stained with three dyes are depicted according to the various detection wavelengths: (a) 516 nm (the emission peak of the green fluorescent), (b) 579 nm (that of the orange fluorescent), (c) 672 nm (that of the dark-red fluorescent), (d) is a mixed image of (a), (b), and (c). The scale bar is 50 μm in size.

FIG. 13. Three types of fluorescent beads are imaged. Yellow-green and orange beads with a 6-μm diameter and deep-red beads with a 1.5-μm diameter are mixed on the glass. Some images of representative wavelengths were taken from (a) to (f). (g) is a mixed image of (b), (c), and (e). The spectra of these beads are shown in (h).

on the detection wavelength. On the other hand, the dotted lines denote the reference data from the fluorescent provider (Invitrogen). The difference between these two lines is apparent in some regions. The mismatch between these two lines is due to the use of a notch-filter to block the reflected laser light perfectly. The rejection bands are shaded in different colors as shown in Fig. 13(h). To exclude these parts, the two lines show a similar tendency.

V. CONCLUSION

In this paper, a confocal-spectral microscope which has the ability to detect the continuous wavelength-dependent images is designed and analyzed. In particular, the detection method is changed. By rotating a single scanning mirror, the wavelength selection becomes more flexible compared to previous products. Using only one PMT, the detection of a broad range is possible. This simple and cost-effective advantage can be utilized for other imaging modalities.

The proposed confocal-spectral microscope utilizes an AOTF to divide its excitation and emission lights. The emission light from a specimen goes through the AOTF without any interaction caused by RF signals. However, a slight difference in the propagating angle arises depending on the polarization state. This difference is offset by an additional birefringent material known as calcite. Also, theoretical and experimental verifications were conducted. Finally, fluorescence beads stained with multiple colors were imaged by this system to confirm whether the spectrum signal follows the original emission spectrum.

[1] T. Zimmermann, J. Rietdorf, and R. Pepperkok, FEBS Lett. **546**, 87–92 (2003).
[2] H. Tsurui, H. Nishimura, S. Hattori, S. Hirose, K. Okumura, and T. Shirai, J. Histochem. Cytochem. **48**, 653–662 (2000).
[3] R. Lansford, G. Bearman, and S. E. Fraser, J. Biomed. Opt. **6**, 311–318 (2001).
[4] R. Borlinghaus and L. Kuschel, Nat. Methods Application note, (2006).
[5] J. H. Frank, A. D. Elder, J. Swartling, A. R. Venkitaraman, A. D. Jeyasekharan, and C. F. Kaminski, J. Microsc. **227**, 203–215 (2007).
[6] J. Engelhardt, U.S. patent 6,614,526 (Sep 2 2003).
[7] W. Knebel, U.S. patent 6,977,724 (Dec 20 2005).
[8] J. M. Larson, Cytometry **69A**, 825–834 (2006).
[9] F. Wu, X. Zhang, J. Y. Cheung, K. Shi, Z. Liu, C. Luo, S. Yin, and P. Ruffin, Biophys. J. **91**, 2290–2296 (2006).
[10] M. Mathew, S. Santos, and D. Zalvidea, Rev. Sci. Instrum. **80**, 073701 (2009).
[11] B. Krämer, V. Buschmann, U. Ortmann, M. Wahl, A. Bülter, F. Koberling, and R. Erdmann, Picoquant Technical Note, 2011.
[12] S. Shrestha, B. E. Applegate, J. Park, X. Xiao, P. Pande, and J. A. Jo, Opt. Lett. **35**, 2558–2560 (2010).
[13] M. S. Roberts, Y. Dancik, T. W. Prow, C. A. Thorling, L. L. Lin, J. E. Grice, T. A. Robertson, K. König, and W. Becker, Eur. J. Pharm. Biopharm. **77**, 469–488 (2011).
[14] L. Bei, G. Dennis, H. Miller, and T. Spaine, Prog. Quantum Electron. **28**, 67–87 (2004).
[15] I. Chang, U.S. Patent 4,052,121 (Oct 4 1977).
[16] I. Song and D.-G. Gweon, in Meas. Sci. Technol. **19**, 085504 (2008).
[17] E. Hecht, *Optics*, 4th ed. (Addision Wesley, San Francisco, 2002), pp. 187–188.